ACS OMEGA

Open Access

http://pubs.acs.org/journal/acsodf

Article

Constructing a $P_2W_{18}O_{62}^{6-}$-Containing Hybrid Photocatalyst via Noncovalent Interactions for Enhanced H_2 Production

Ruonan Li, Rui Chen, Linxia Tang, Qing Li, Yan-Xin Chen,* Jinsheng Liao,* and Wei Wang*

Cite This: *ACS Omega* 2024, 9, 18556−18565

Read Online

ACCESS | Metrics & More | Article Recommendations | Supporting Information

ABSTRACT: Polyoxometalates (POMs) have gained significant research attention because of their excellent properties in photocatalytic (PC) hydrogen production. Exploring POM-based compounds for heterogeneous photocatalysis is an ongoing task. Here, we obtain a water-insoluble inorganic−organic hybrid compound, $(P_2W_{18}O_{62})_3(C_{12}N_3H_{10})_6(C_{12}N_3H_{11})_6{\cdot}9.5H_2O$ (P-PW), formed by Dawson-type POM $P_2W_{18}O_{62}^{6-}$ (P_2W_{18}) anions and protonated 2-(pyridin-4-yl)-1*H*-benzo[*d*]imidazole (PHB) cations via noncovalent interactions. In the presence of the sacrificial agent triethanolamine, P-PW exhibits a PC H_2 generation rate of 0.418 mmol/g/h, surpassing that of P_2W_{18} and PHB by 15 and 17 times, respectively. This enhancement in PC performance of P-PW can be attributed to its band structure change from the precursor compounds, leading to increased light absorption and therefore more efficient PC hydrogen production.

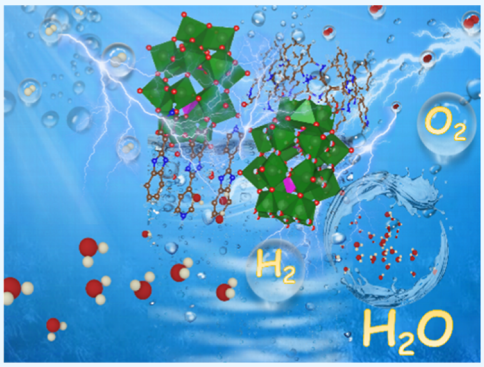

1. INTRODUCTION

According to a recent report by the Intergovernmental Panel on Climate Change (IPCC), the CO_2 emission from fossil-fuel combustion and industrial processes account for about two-thirds of global greenhouse gas emissions.[1] Clearly, our choice of energy sources is at the heart of climate/environmental issues.[2] The realization of a carbon-neutral future relies on reforming the energy structure, which urges the exploration of sustainable energy resources to replace fossil fuels. Among different alternative energy options, photocatalysis has gained widespread attention and research interests.[3,4] The principle of this technology involves the absorption of solar energy by a photocatalyst, which then activates the dissociation of water molecules and produces H_2 and O_2.[5−8] The production of hydrogen fuel in this process does not emit carbon dioxide, making the generated hydrogen gas a clean energy supply. With the continuous in-depth research on the photocatalytic (PC) processes, it is believed that H_2 production from photocatalysis might be a promising solution for the renewable energy challenge.[9,10]

To improve the performance of photocatalysis, it is critical to consider the material choice and structural design of the photocatalysts. Traditional noble metal catalysts (e.g., Pt, Rh, and Ir and their oxides)[11,12] are too expensive for large-scale applications.[13] To lower the cost, earth-abundant transition-metal-based compounds have been explored extensively.[14−18] Among different materials, polyoxometalate (POM) compounds exhibit a wide variety of elemental compositions and versatile molecular structures, leading to their interesting physical and chemical properties.[4,6,19−25] Among many types of POMs, the Wells−Dawson type, with the general formula $[X_2M_{18}O_{62}]^{n-}$, has been widely exploited for PC water splitting reactions because of their ease of synthesis and unique chemical/electron-transfer properties. For example, Duan and co-workers have reported a variety of Wells−Dawson-type POMs embedded in the pores of REDOX-active coordination polymers or other material matrixes for PC hydrogen evolution.[26,27] They have shown that the Dawson-type P_2W_{18} polyanion plays a key role in affecting the rate of hydrogen evolution by synergistically interacting with other substances. Lin and co-workers incorporated $[P_2W_{18}O_{62}]^{6-}$ onto a Zr-based MOF sensitized by $[Ru(bpy)_3]^{2+}$ to achieve hydrogen production under visible light.[28] They also encapsulated a cobalt-containing Dawson-type POM into MIL-101 with photosensitizer for PC H_2 productions.[29] Nevertheless, it is important to notice that early research studies of POMs as photocatalysts often show limited light adsorption[30,31] and required noble metal cocatalysts to boost their activity.[32,33] The development of noble-metal-free POM-based photocatalysts that function under the solar spectrum is a substantial need.

It is well-known that ligand plays a key role in the construction of functional coordination compounds, which demonstrates interesting properties in fluorescence recognition,[34] sensing,[35] chemical catalysis, and photocatalysis.[36,37] Compounds with pyridinyl benzimidazole ligands have been explored in various

Received: February 5, 2024
Revised: March 13, 2024
Accepted: March 21, 2024
Published: April 9, 2024

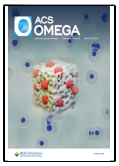

reactions.[38,39] In this work, to obtain an efficient hydrogen evolution photocatalyst, we cocrystallize the Dawson-type POM $P_2W_{18}O_{62}^{6-}$ with 2-(pyridin-4-yl)-1*H*-benzo[*d*]imidazole pyridyl benzimidazole to form a hybrid compound $(P_2W_{18}O_{62})_3(C_{12}N_3H_{10})_6(C_{12}N_3H_{11})_6{\cdot}9.5H_2O$ (P-PW). This hybrid compound is stabilized via noncovalent interactions, leading to a water-insoluble POM-based photocatalyst. The PC properties of P-PW are further characterized, with its band structure being analyzed based on photoelectrochemical (PEC) characterizations and Mott−Schottky analysis.

2. EXPERIMENTAL SECTION

2.1. Materials. 2-(Pyridin-4-yl)-1*H*-benzo[*d*]imidazole (98% purity) was purchased from Bide Pharmatech Ltd. (Shanghai, China). $Na_2WO_4{\cdot}2H_2O$ (98% purity), KCl (99% purity), and NaOH (96% purity) were obtained from Shanghai Adamas Reagent Co., Ltd. (Shanghai, China) and used without further purification. FTO conductive glass was purchased from Hunan Xiangcheng Instrument. Ultrapure water was used throughout the experiment. Concentrated HCl and H_3PO_4 were obtained from Sinopharm Group Chemical Reagent Co., Ltd. (Shanghai, China); they were of analytical grade and used without further purification.

2.2. Synthesis of α-$K_6P_2W_{18}O_{62}{\cdot}14H_2O$. The synthesis of α-$K_6P_2W_{18}O_{62}{\cdot}14H_2O$ was conducted following a previously reported procedure.[40] In specific, $Na_2WO_4{\cdot}2H_2O$ (300 g; 0.91 mol) was first dissolved in 350 mL of ultrapure water. Under intense agitation, an HCl solution (250 mL, 4.0 mol/L) was added dropwise to the $Na_2WO_4{\cdot}2H_2O$ solution, generating white suspended solids. After the turbid solution turned clear, the H_3PO_4 solution (250 mL, 4.0 mol/L) was subsequently added drop by drop, changing the solution from colorless to light green. After the addition of the H_3PO_4, the clear solution was refluxed at 100 °C for at least 24 h, during which the solution gradually turned dark green. The solution was cooled to room temperature, and 150 g of KCl was added to form an immediate precipitation. After stirring for additional 10 min, the insoluble matter was filtered and then dried at 60 °C overnight. The crude product was dissolved in 650 mL of ultrapure water, and the obtained solution was filtered. The filtrate was refluxed at 80 °C for 72 h, cooled to room temperature, and placed in a refrigerator at 4 °C. After 24 h, light-green crystals of block shapes can be collected as α-$K_6P_2W_{18}O_{62}{\cdot}14H_2O$.

2.3. Synthesis of $(P_2W_{18}O_{62})_3(C_{12}N_3H_{10})_6(C_{12}N_3H_{11})_6{\cdot}9.5H_2O$. 5.0 g portion of α-$K_6P_2W_{18}O_{62}{\cdot}14H_2O$ and 1.0 g of 2-(pyridin-4-yl)-1*H*-benzo[*d*]imidazole (PHB) were dissolved in 350 mL of water. The mixture was stirred for 30 min and filtered to remove insoluble matter. The clear solution was placed in an oil bath at 100 °C and evaporated to dryness to obtain the yellow hexagonal lamellar crystal $(P_2W_{18}O_{62})_3(C_{12}N_3H_{10})_6(C_{12}N_3H_{11})_6{\cdot}9.5H_2O$ (P-PW).

2.4. Characterization. Single crystals without cracks or defects were selected under an optical microscope for an X-ray crystallography study. The data was collected at 100 K on a Bruker D8 VENTURE equipped with a microfocus Mo Kα radiation. The Bruker APEX program was used to perform the data reduction, and Olex 2−1.5[41] software with built-in SHELXL[42] and PLATON[43] programs was used for structure analysis and refinement. The final structure file was uploaded to the CCDC database (No. 2330807). To visualize the noncovalent interactions in the structure, the electronic wave function was generated by the PM6 method with the Gaussian 16 program,[44] and then the interaction region indicator (IRI) analysis[45] was performed with the Multiwfn package.[46]

X-ray photoelectron spectroscopy (XPS) was studied on a ThermoFisher ESCALAB 250 Xi system, with a 284.8 eV C 1s spectral line as binding energy correction, and XPS Peak41 software was used for peak fitting. Thermogravimetric analyses (TGA) were performed on a thermal analysis instrument (Mettler-Toledo TGA/DSC 1) from room temperature to 1000 °C with a heating rate of 5 °C/min under an Ar atmosphere. Powder X-ray diffraction (PXRD) patterns were collected on a Rigaku Miniflex 600 diffractometer with Cu Kα radiation in the 2θ range of 3−60° with a step size of 0.02°. A Le Bail[47,48] fit was performed using the *FULLPROF* suite.[49] 2θ zero shift and unit cell parameters were allowed to vary for the refinement. The infrared spectra were recorded on a Nicolet iS50 spectrometer with ATR mode in the range of 4000−525 cm^{-1} at room temperature. Optical diffuse reflectance and UV−vis spectra were recorded at room temperature on an Agilent Cary 5000 UV−vis−NIR spectrophotometer. The PC reaction was carried out under irradiation with the Microsolar 300 Xe lamp (Beijing Perfectlight Technology Co., Ltd.). The generated H_2 was analyzed periodically by an FULI-GC-9790II gas chromatograph (GC) (Zhejiang Fuli Analytical Instrument Co., Ltd.) equipped with a thermal conductivity detector (TCD).

2.5. EC and PEC Measurements. To fabricate the electrode, 10 mg of photocatalyst was mixed with 0.5 mL of ultrapure water, followed by sonication for 30 min to ensure a uniform dispersion. Subsequently, 25 μL of 25% Nafion was added to the mixture, which was sonicated for 1 h. 50 μL of the mixture suspension was applied evenly onto a piece of FTO conductive glass (electrode area: 1 cm^2). The electrode was dried in ambient conditions overnight. The load of catalysts was determined by subtracting the initial weight of the glass from the electrode's final weight.

All electrochemical (EC) and photoelectric measurements were conducted in a standard three-electrode system, with the catalyst-loaded electrode as the working electrode, a Ag/AgCl electrode (in saturated KCl solution) as the reference electrode, and a piece of Pt metal sheet (1 × 1 cm^2) as the counter electrode. 0.1 M Na_2SO_4 solution (pH = 6) was chosen as the electrolyte. Linear sweep voltammetry (LSV) and chronoamperometry (I−t) analyses were conducted on a CHI-760E EC workstation. A high-uniformity integrated Xe light source (PLS-FX300HU, Beijing Perfectlight, Beijing, China) with an AM 1.5 G filter (100 mW/cm^2) was employed as the light source. A customized reactor with a window was adopted for the measurement. During the PEC process, the light emitted from the xenon lamp was irradiated directly onto the surface of the working electrode through the window.

LSV is widely used to test the variation of photocurrent with voltage, which further determines the light conversion efficiency of the photoanode. In this paper, the photocurrent density generated by the photoanode under illumination and simultaneously applied bias was tested, and the corresponding photoelectric conversion efficiency was calculated. For the measurement, the voltage range was varied from −0.45 to 1.0 V (vs Ag/AgCl), and the scan rate was set to 5 mV/s. To eliminate the influence of the pH of the electrolyte, the potential was converted to the value referencing the standard reversible hydrogen electrode potential (RHE). The calculation was done based on the Nernst equation, which is shown in eq 1.

$$E_{RHE} = E_{Ag/AgCl} + 0.0592 \times pH + E^0_{Ag/AgCl} \quad (1)$$

https://doi.org/10.1021/acsomega.4c01179
ACS Omega 2024, 9, 18556−18565

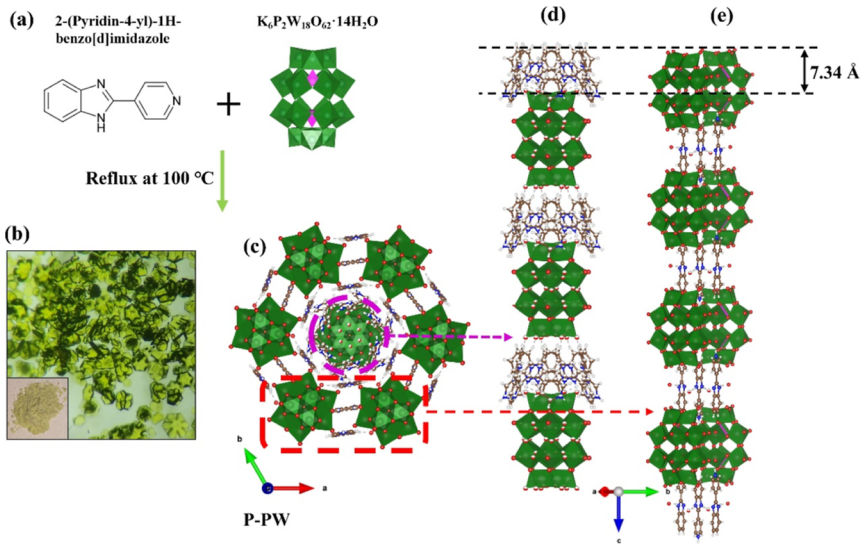

Figure 1. (a) Synthetic route of P-PW; (b) powder and single-crystal morphology of P-PW; (c) P-PW structure stacking diagram; (d) the unordered part expands in the *c* direction; and (e) the ordered part expands in the *c* direction. Color code: WO_6 octahedron—dark green polyhedra, PO_4 tetrahedron—pink polyhedra, C—gray, O—red, N—blue, and H—white.

where $E^0_{Ag/AgCl}$ equals 0.1976 V vs RHE at room temperature.

The $I-t$ curve was used to study the stability of photocurrent at a constant voltage with and without illumination. The voltage was set to 0.6 V (vs Ag/AgCl), and the illumination cycle time was chosen as 300 s (i.e., each cycle performs the light-off measurement for 300 s and then the light-on measurement for 300 s). The measurement was conducted for a total of 3600 s.

The incident monochromatic photon-electron conversion efficiency (IPCE) was measured using the chronoamperometric method (potentiostatic method) in the IPCE1000 system (Beijing Perfectlight Technology Co., Ltd.). This system allows for the application of a bias between the working electrode and the counter electrode (in a 2-electrode experiment) or the reference electrode (in a 3-electrode experiment), while simultaneously measuring the current generated by the PEC electrode under monochromatic light of varying wavelengths. The discrepancy between the steady-state current and the steady-state background current under monochromatic illumination arises from the photocurrent generated by the oxidation–reduction reaction on the surface of the working electrode. IPCE is calculated as the ratio of the photocurrent (converted to electron rate) to the incident photon rate (derived from the calibrated power of the light source). For this experiment, calibrated monochromatic light with a wavelength step of 1 nm, a wavelength range of 300–600 nm, and an effective optical area of 1 × 1 cm^2 is utilized. The relationship between the IPCE and the wavelength, denoted as λ (nm), is illustrated by eq 2.

$$\text{IPCE}\ (\%) = \frac{1240 \times J_p}{\lambda \times I_0} \times 100\% \tag{2}$$

where J_p represents the photocurrent density recorded at a given wavelength, λ denotes the specific wavelength, and I_0 stands for the intensity of the incoming light.

The Mott–Schottky analyses were utilized to delineate the flat band potentials, typically corresponding to the position of the semiconductor conduction band. The EC analyzer encompasses a frequency range of 0.01 to 100,000 Hz, with a voltage increment of 0.005 V and an AC amplitude of 10 mV. The working electrode was analyzed at frequencies of 500, 1000, 1500, 2000, and 2500 Hz, respectively. The Schottky barrier serves to denote the conduction band potential position and facilitates computation of the flat band potential. The computational expression of the Mott–Schottky model, based on parallel plate capacitors, is encapsulated in eq 3.

$$\frac{1}{C_{SC}^2} = \frac{2}{\varepsilon\varepsilon_0 q N_D}\left(E_{appl} - E_{FB} - \frac{kT}{q}\right) \tag{3}$$

In the parallel plate capacitor model, C_{sc} represents the space charge layer capacitance; ε stands for the relative dielectric constant of the semiconductor; ε_0 is the dielectric constant of vacuum; N_D stands for the carrier concentration; E_{appl} is the applied bias; E_{FB} is the flat band potential; k is the Boltzmann constant; and T represents the temperature. The value of E_{FB} can be determined based on where the $\frac{1}{C_{SC}^2}$-E_{appl} line intercepts the E_{appl} axis.

For measuring the EC impedance spectroscopy, the testing frequency was between 10 mHz and 100 kHz. The Nyquist plot tends to show a twisted semicircular curve with or without a straight tail. The shape of the curve may be influenced by the EC characteristics of the electrode and the electrolyte, as well as the experimental conditions.

2.6. PC Hydrogen Evaluation. The PC H_2 evolution experiments were conducted on an automatic all-glass online trace gas analysis system (Labsolar-6A, Beijing Perfectlight Technology Co., Ltd.) using a xenon lamp (Microsolar 300, with an AM 1.5 G filter and calibrated to 100 mW/cm^2). Typically, 20 mg of each photocatalyst was added to 100 mL of an aqueous solution containing triethanolamine (TEOA) (50% volume ratio) as the sacrificial agent. The mixture was sealed in a glass vessel with a quartz window on top, and the mixture was stirred continuously during the photoreaction. By using a water-cooling system, the solution temperature was controlled at 5 °C. After degassing, the vessel was irradiated by the Microsolar 300 xenon lamp. The generated H_2 was analyzed periodically by a FULI-GC-9790II GC (ZhejiangFuli Analytical Instrument Co., Ltd.) equipped with a TCD. Argon (Ar) was used as the carrier gas, and the flow rate was set to 30 mL/min.

https://doi.org/10.1021/acsomega.4c01179
ACS Omega 2024, 9, 18556–18565

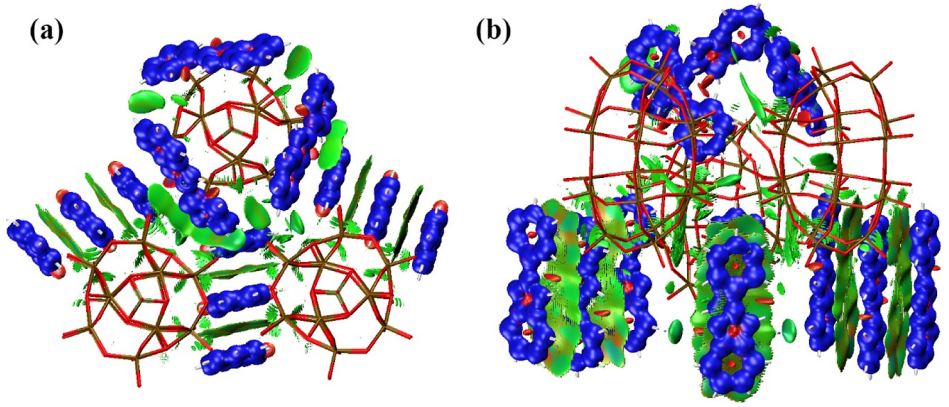

Figure 2. IRI analysis of the P-PW structure, showing the noncovalent interactions between the PHB cations (a) in the concaved "cyclone-cone" and (b) between the ordered columns.

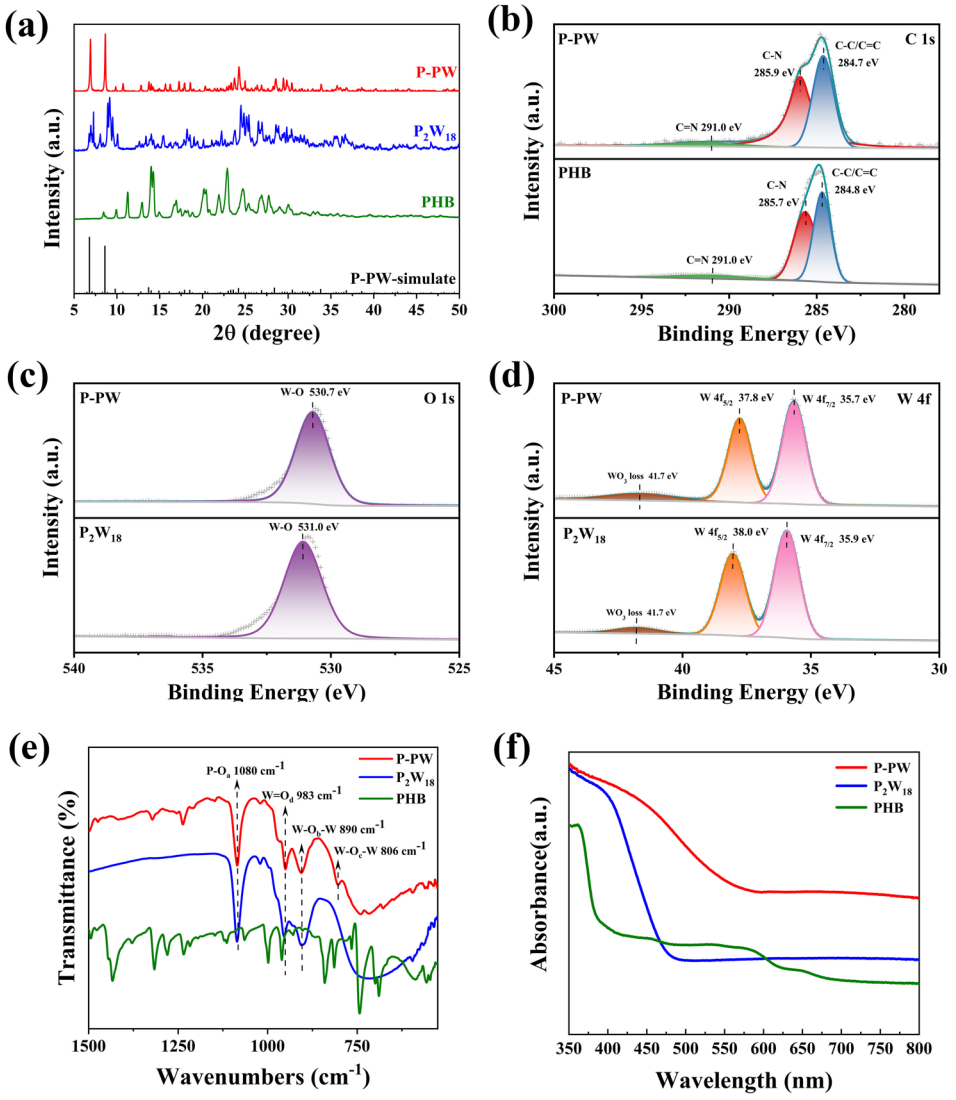

Figure 3. Characterization of PHB, P_2W_{18}, and P-PW: (a) PXRD; (b–d) XPS analysis; (e) FT-IR spectra; and (f) UV–visible spectra.

3. RESULTS AND DISCUSSION

3.1. Description of the Crystal Structure. The reaction between 2-(pyridin-4-yl)-1*H*-benzo[*d*]imidazole (PHB) and α-$K_6P_2W_{18}O_{62}\cdot 14H_2O$ (P_2W_{18}) results in the formation of a new compound P-PW, as shown in Figure 1a,b. The cif file is provided as Supporting Information. Single-crystal X-ray diffraction reveals that P-PW possesses a *P6* space group, with the following unit cell parameters: $a = b = 20.58$ Å, $c = 18.83$ Å, $\alpha = \beta = 90°$, $\gamma = 120°$, and V = 6908 Å^3. The asymmetric unit of the

https://doi.org/10.1021/acsomega.4c01179
ACS Omega 2024, 9, 18556−18565

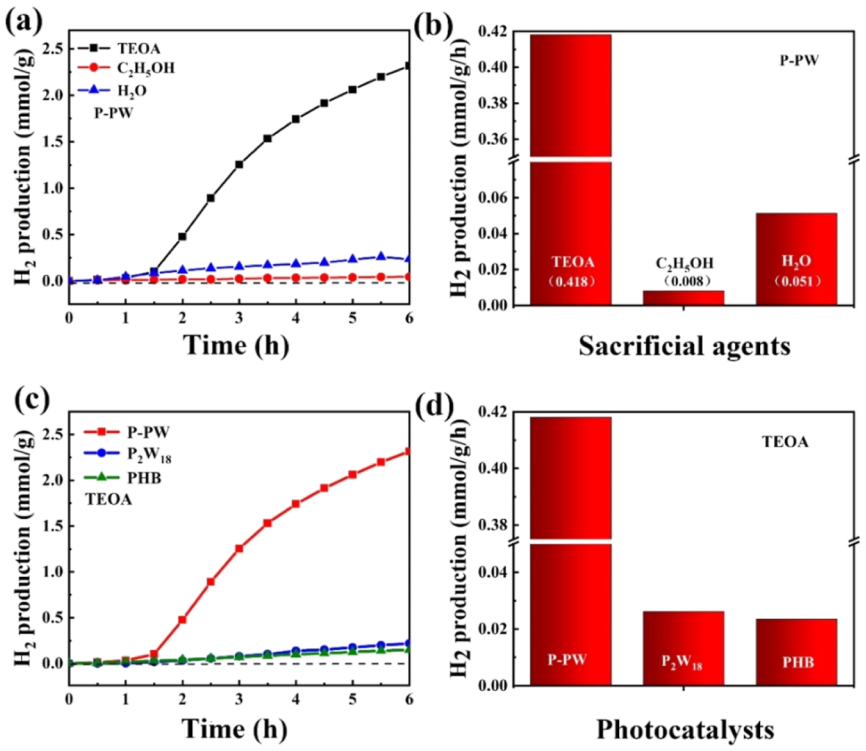

Figure 4. (a) Effect of different sacrificial agents on the hydrogen production of P-PW; (b) effect of different sacrificial agents on the hydrogen production rate of P-PW at 3 h; (c) 6 h hydrogen production for P-PW, P_2W_{18}, and PHB in an aqueous solution containing 50% volume of TEOA as a sacrificial agent; (d) hydrogen production rate of P-PW, P_2W_{18}, and PHB within 3 h (1:1 volume of H_2O and TEOA).

P-PW consists of half of a $P_2W_{18}O_{64}^{6-}$ polyanion and half of a protonated PHB cation, as depicted in Figure S1. Viewing from the *c* axis, we can see that the $P_2W_{18}O_{64}^{6-}$ anions form columns along the [001] direction, and these columns further form a 2D closed-pack structure in the a−b plane (Figure S2). A group of seven $P_2W_{18}O_{64}^{6-}$ columns are chosen to further illustrate the structure (Figure 1c). We can see that the outer six columns consist of ordered $P_2W_{18}O_{64}^{6-}$, but the $P_2W_{18}O_{64}^{6-}$ in the middle column is all disordered over two positions (each with 50% occupancy). In the central column, there are three protonated PHB cations positioned head-to-toe above each $P_2W_{18}O_{64}^{6-}$ anion, forming an upside-down "cyclone-cone" (Figure 1d). Figure S3 shows one set of the two equally occupied disordered structures for P-PW. The "cyclone-cone" is also disordered into two different positions, with the concave side covering the $P_2W_{18}O_{64}^{6-}$ anion. Meanwhile, the $P_2W_{18}O_{64}^{6-}$ polyanions are ordered in the six outer columns, with six sets of three parallel stacking PHB cations positioned between each two columns (Figure 1e). It is worth pointing out that the $P_2W_{18}O_{64}^{6-}$ anion in the outer columns is displaced by 7.34 Å along the *c*-axis from the nearby $P_2W_{18}O_{64}^{6-}$ anion in the central column.

The P-PW structure is held together by noncovalent interactions. To visualize the noncovalent interactions in the P-PW structure, we conduct the IRI analysis on a representative fragment of the P-PW structure (Figure 2). According to the definition of IRI analysis, the interacting region between different components can be color-coded according to their indicator values.[45] For example, the green region stands for attractive interactions, while the red region consists of repulsive interactions. As shown in Figure 2, we can see that strong attractive interactions can be found between the PHB cations in the structure. Between the three PHB cations in the "cyclone cone", the attractive nature comes from the off-90-degree T-shape aromatic interactions (Figure 2a). On the other hand, off-center $\pi-\pi$ stacking interactions are found between the parallel PHB cations stacks positioning between the $P_2W_{18}O_{64}^{6-}$ columns (Figure 2b). Furthermore, attractive interactions are also found between the "cyclone cones" and the parallel stacks, which complete the noncovalent interaction network between all PHB cations. This extensive network of noncovalent interactions makes P-PW insoluble in most solvents, except *N*,*N*-dimethylformamide.

3.2. Characterization of the P-PW Polycrystalline Powders. Additional characterizations are performed on the polycrystalline powder of P-PW. Figure 3a displays the X-ray diffraction pattern of the P-PW polycrystalline powder. The experimental pattern matches well with the simulated pattern from the single-crystal structure. The Le Bail fit (with χ^2 of 1.18%) proves that the structure determined by single-crystal X-ray diffraction is representative of the powder, and no crystalline impurities are observed. The fitting results are shown in Figure S4. Unit cell parameters obtained by the Le Bail fit are as follows: a = 20.66 Å, b = 20.66 Å, c = 18.79 Å, α = 90°, β = 90°, and γ = 120°. These results confirm that the polycrystalline powder is phase pure and exhibits good crystallinity. XPS is an important tool for the determination of the elemental composition and oxidation state in samples. Figure S5 shows the full XPS spectra of P-PW crystalline powder, and the high-resolution XPS spectra of P_2W_{18}, PHB, and P-PW are shown in Figure 3b−d. The C 1s spectra of PHB and P-PW are similar, indicating that the chemical nature of PHB cations does not change significantly in the P-PW hybrids. The corresponding characteristic peak positions can also be found for both C−N and C═N. The O 1s spectra of P-PW and P_2W_{18} are similar, indicating that the chemical properties of POM and P_2W_{18} monomers in P-PW

https://doi.org/10.1021/acsomega.4c01179
ACS Omega 2024, 9, 18556−18565

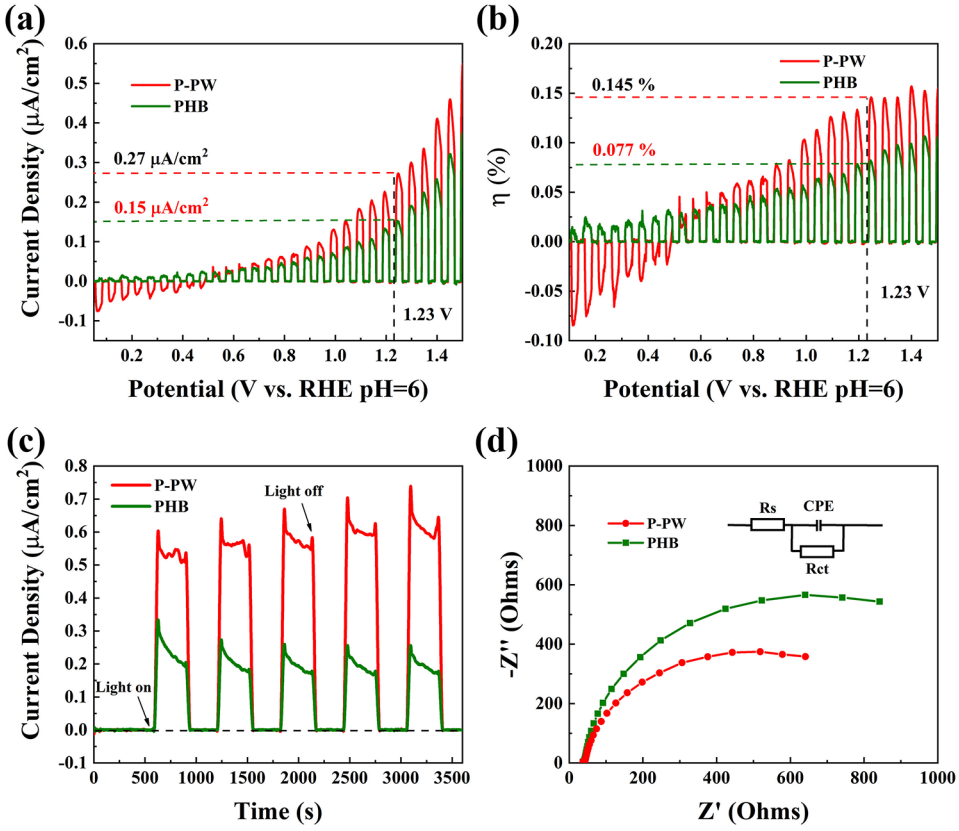

Figure 5. (a) LSV curve of P-PW and PHB photoanodes under cyclic switching, (b) photoelectric conversion efficiency of P-PW, PHB η curve, (c) $I-t$ curve of P-PW and PHB photoanodes, and (d) EC impedance spectroscopy of P-PW and PHB.

hybrids remain similar. The binding energies of W $4f_{7/2}$ and W $4f_{5/2}$ of P-PW are 35.7 and 37.8 eV, respectively, with the corresponding values of P_2W_{18} being 35.9 and 38.0 eV. The spin−orbit splitting value of 2.1 eV corresponds to the +6 oxidation state of W in both compounds. The 41.7 eV signal corresponds to the energy loss peak of WO_3. Figure 3e shows the FT-IR spectra of P-PW, PHB, and α-$K_6P_2W_{18}O_{62}\cdot 14H_2O$ (P_2W_{18}). The absorption signals at 1080, 983, 890, and 806 cm^{-1} can be attributed to P−O_d, W−O_b, W−O_b−W, and W−O_c−W vibrations, respectively. The peaks at 1322, 1215, 1151, 741, and 557 cm^{-1} are shared between P-PW and PHB.[50−52]

The optical absorption of P-PW is studied by UV−vis spectroscopy (Figure 3f), with the spectra of PHB and α-$K_6P_2W_{18}O_{62}\cdot 14H_2O$ (P_2W_{18}) also collected as comparisons. The absorption of P_2W_{18} occurs mostly in the UV range, and its visible absorption is limited to the purple region. PHB, on the other hand, exhibits optical absorption covering almost the whole visible spectrum. Therefore, by combining PHB with P_2W_{18}, it is expected that P-PW exhibits noticeable absorption up to 550 nm, which is improved compared with P_2W_{18}. This property could be beneficial for PC properties.

3.3. PC, PEC, and EC Performance. As shown in Figure 4a,b, the PC activity of P-PW was studied in water with and without sacrificial agents. The results indicate that the hydrogen production rate in pure water (0.008 mmol/g/h) is even higher than in ethanol (0.051 mmol/g/h), revealing that ethanol may not be an excellent sacrificial agent for P-PW. On the contrary, the hydrogen production rate by P-PW in TEOA aqueous solution (0.418 mmol/g/h) is significantly higher than that in pure water, highlighting the importance of sacrificial agents as the hole scavenger in preventing the reverse reactions and electron−hole recombination in PC reactions. The PC hydrogen evolution activity of P-PW is then conducted under simulated solar radiation in an aqueous solution containing 50% volume of TEOA as the sacrificial agent. PHB and P_2W_{18} are also characterized for comparison. As shown in Figure 4c,d, the hydrogen production rate of P-PW (0.418 mmol/g/h) is greatly enhanced (by more than 15 times) from that of P_2W_{18} and PHB, which are only 0.029 and 0.024 mmol/g/h, respectively. Unlike most reported POM-based photocatalysts, which require precious metal cocatalysts or fluorescent groups to enhance their performance, P-PW exhibits excellent PC properties by simply combining PHB and $P_2W_{18}O_{64}^{6-}$ anions.

Because of the high solubility of P_2W_{18} in water, we cannot produce electrodes that are stabilized in the electrolyte (0.1 M Na_2SO_4 solution, pH = 6). Therefore, for photoelectrochemical measurements, we only characterize the properties of PHB and P-PW. The LSV measurements are typically conducted within the potential range of 0.1 to 1.5 V (vs RHE) with a scan rate of 5 $mV\cdot s^{-1}$. The light is cut off at a rate of 5 s^{-1}, as shown in Figure 5a, to realize alternating illumination. The photocurrent density of P-PW at 1.23 V (vs RHE) is 0.27 $\mu A/cm^2$, which is 1.8 times higher than that of PHB (0.15 $\mu A/cm^2$). The significant increase in photocurrent might be attributed to the enhanced charge-separation between the PHB cations and $P_2W_{18}O_{64}^{6-}$ anions, resulting in the robust photocurrent response in P-PW. Photoelectric conversion efficiency (η) is calculated based on the photocurrent density of the photoanodes, as shown in Figure 5b. Under full spectrum irradiation, the P-PW photoanode can achieve an optimal photoelectric

https://doi.org/10.1021/acsomega.4c01179
ACS Omega 2024, 9, 18556−18565

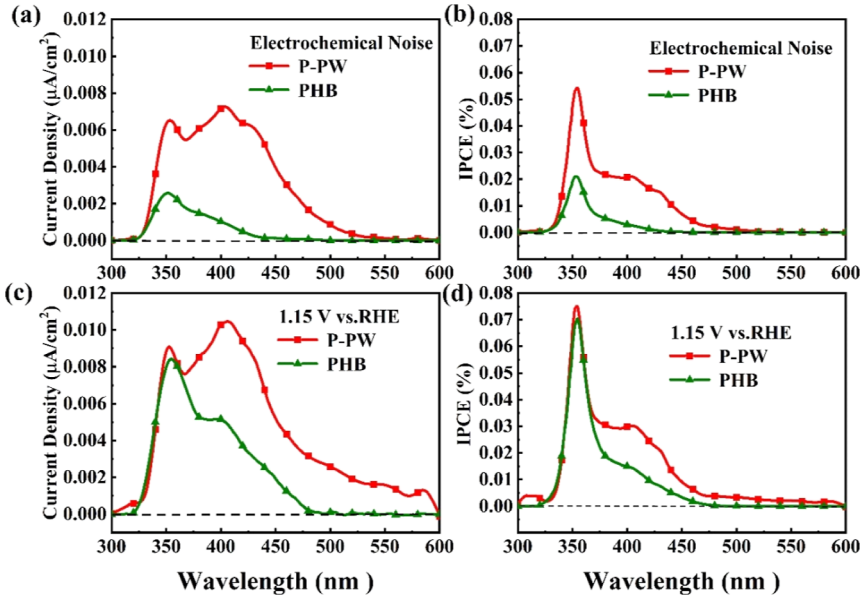

Figure 6. (a) Correlation between photocurrent density and monochromatic light was studied using EC noise mode; (b) IPCE (%) spectrum is generated based on photocurrent density and monochromatic light data; (c) correlation between photocurrent density and monochromatic light at 1.15 V (vs RHE); (d) IPCE (%) spectrum.

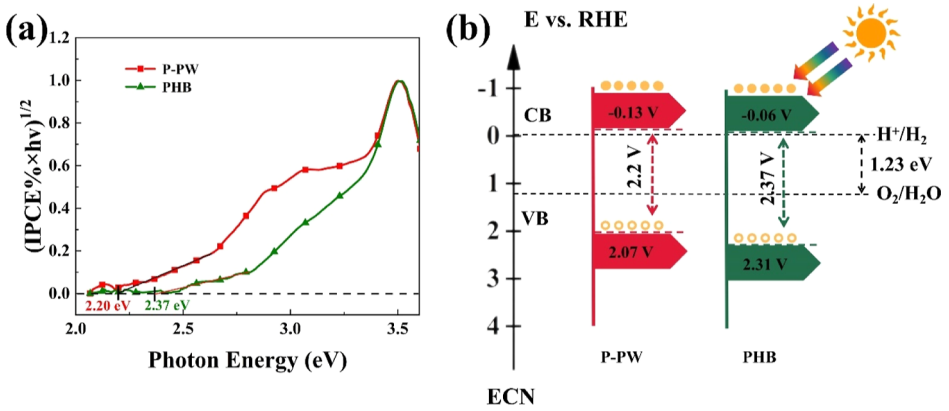

Figure 7. (a) Band gap determination was obtained by analyzing the IPCE spectra, specifically by examining the relationship between (IPCE % × hv)$^{1/2}$ vs hv; (b) proposed band structures of the pure P-PW and PHB.

conversion efficiency of 0.145% at a bias voltage of 1.23 V (vs RHE), which is almost twice of the PHB photoanode (0.077%, at 1.23 V vs RHE). Chromatoamperometric measurements are performed at 1.23 V vs RHE in 0.1 M Na_2SO_4 solution to check the chemical stability of the samples, as shown in Figure 5c. Compared with PHB, which shows a photocurrent density of 0.26 $\mu A/cm^2$, P-PW exhibits a much higher photocurrent density (0.6 $\mu A/cm^2$) during the light-on/light-off cycles. The increased photocurrent density is stable throughout the extended cycle, indicating the excellent photostability of P-PW. Further analysis by electrochemical impedance spectroscopy (EIS) reveals that the charge transfer resistance of P-PW is lower than that of PHB (Figure 5d). The lower charge transfer resistance of P-PW likely enables faster electron transfer during the PEC process, thereby enhancing the PC activity of the water splitting.

To further investigate the absorption intensity and photoelectric conversion efficiency of the sample under different wavelengths of light during the reaction, we utilized the electrochemical noise (ECN) mode to measure the photocurrent densities. This nondestructive and in situ monitoring technique allows for the investigation of spontaneous EC reactions that occur at the photoanode under illumination (Figure 6). As a result, significant visible light absorption of P-PW in the 300−580 nm range can be observed, while PHB shows little response in the visible range. Specifically, P-PW exhibits a distinct absorption peak at 420 nm. These findings confirm that the cocrystallization of PHB and P_2W_{18} into P-PW significantly enhances visible light absorption (Figure 6a).

IPCE is defined as the ratio of the number of electrons flowing through a closed circuit to the number of photoelectrons in the incident monochromatic light. It is employed to assess the photoelectric conversion efficiency at different wavelengths and is regarded as one of the key indicators for evaluating the PEC performance of photoelectrodes. Owing to the distinct responses of semiconductor materials to incident light of varying wavelengths, the measurement of IPCE for a photoelectrode provides a more accurate evaluation of the utilization of monochromatic photons by the photoelectrode. Figure 6b shows the IPCE spectrum based on the photocurrent wavelength curve. P-PW shows the highest IPCE value (0.055%) at the 350 nm region and reaches 0.025% at 420 nm, confirming

https://doi.org/10.1021/acsomega.4c01179
ACS Omega 2024, 9, 18556−18565

the response of P-PW to visible light. Upon applying a bias voltage of 1.15 V (vs RHE), the photocurrent, IPCE, and monochromatic radiation characteristics of P-PW are measured and depicted in Figure 6c,d. The photocurrent response of P-PW increases with increasing bias. Under 420 nm illumination, the photocurrent is 1.4 times that of PHB, while the IPCE is 0.075 and 0.035% at 350 and 420 nm, respectively. These improvements are consistent with the LSV curve results.

According to the IPCE spectra, the band gap (Eg) values of P-PW and PHB can be derived as 2.20 and 2.37 eV, respectively (as shown in Figure 7a). In addition, Mott−Schottky measurements are conducted to investigate the band structures of the prepared samples (as shown in Figure S6). The flat band potentials of P-PW and PHB are calculated to be −0.13 and −0.06 V, respectively. Compared with PHB, P-PW exhibits a more negative flat band potential. Based on the flat band potential, the relevant semiconductor band structures of these samples are deduced and summarized, as shown in Figure 7b. The decreased band gap contributes to the increasing light absorption and therefore benefits the PC performance.

4. CONCLUSIONS

In summary, we synthesize a stable POM-based hybrid compound, P-PW, by exploiting the noncovalent interactions between POMs and 2-(pyridin-4-yl)-1*H*-benzo[*d*]imidazole. The PC hydrogen production behaviors of the hybrid compound are analyzed. With TEOA as the sacrificial agent, P-PW exhibits a PC H_2 generation rate of 0.418 mmol/g/h, surpassing that of P_2W_{18} and PHB by 15 and 17 times, respectively. This enhancement in the PC performance of P-PW is attributed to the increasing light adsorption of the hybrid compound as well as the band structure modulation induced by the chemical structure. The hybrid material exhibits good thermal and chemical stability, which might offer a promising approach for the development of stable and efficient POM-based heterogeneous photocatalysts.

■ ASSOCIATED CONTENT

Supporting Information

The Supporting Information is available free of charge at https://pubs.acs.org/doi/10.1021/acsomega.4c01179.

Additional figures of molecular structure, XPS spectra, Le Bail fitting of powder XRD patterns, Mott−Schottky plots, and summary of single-crystal data (PDF)

Crystallographic Information File of P-PW (CIF)

■ AUTHOR INFORMATION

Corresponding Authors

Yan-Xin Chen − *Fujian Institute of Research on the Structure of Matter, Chinese Academy of Sciences, Fuzhou 350108 Fujian, China; Xiamen Institute of Rare-earth Materials, Haixi Institutes, Chinese Academy of Sciences, Xiamen 361021 Fujian, China; Fujian College, University of Chinese Academy of Sciences, Fuzhou 350002 Fujian, China;* orcid.org/0000-0003-1828-3574; Email: yanxinchen@fjirsm.ac.cn

Jinsheng Liao − *School of Chemistry and Chemical Engineering, Jiangxi University of Science and Technology, Ganzhou 341000, China;* orcid.org/0000-0002-0797-5332; Email: jsliao1209@126.com

Wei Wang − *Fujian Institute of Research on the Structure of Matter, Chinese Academy of Sciences, Fuzhou 350108 Fujian, China; Xiamen Institute of Rare-earth Materials, Haixi Institutes, Chinese Academy of Sciences, Xiamen 361021 Fujian, China; Fujian College, University of Chinese Academy of Sciences, Fuzhou 350002 Fujian, China;* orcid.org/0000-0003-3178-236X; Email: wangwei@fjirsm.ac.cn

Authors

Ruonan Li − *School of Chemistry and Chemical Engineering, Jiangxi University of Science and Technology, Ganzhou 341000, China; Fujian Institute of Research on the Structure of Matter, Chinese Academy of Sciences, Fuzhou 350108 Fujian, China; Xiamen Institute of Rare-earth Materials, Haixi Institutes, Chinese Academy of Sciences, Xiamen 361021 Fujian, China; Fujian College, University of Chinese Academy of Sciences, Fuzhou 350002 Fujian, China*

Rui Chen − *Fujian Institute of Research on the Structure of Matter, Chinese Academy of Sciences, Fuzhou 350108 Fujian, China; Xiamen Institute of Rare-earth Materials, Haixi Institutes, Chinese Academy of Sciences, Xiamen 361021 Fujian, China; Fujian College, University of Chinese Academy of Sciences, Fuzhou 350002 Fujian, China*

Linxia Tang − *Fujian Institute of Research on the Structure of Matter, Chinese Academy of Sciences, Fuzhou 350108 Fujian, China; Xiamen Institute of Rare-earth Materials, Haixi Institutes, Chinese Academy of Sciences, Xiamen 361021 Fujian, China; Fujian College, University of Chinese Academy of Sciences, Fuzhou 350002 Fujian, China*

Qing Li − *Fujian Institute of Research on the Structure of Matter, Chinese Academy of Sciences, Fuzhou 350108 Fujian, China; Xiamen Institute of Rare-earth Materials, Haixi Institutes, Chinese Academy of Sciences, Xiamen 361021 Fujian, China; Fujian College, University of Chinese Academy of Sciences, Fuzhou 350002 Fujian, China*

Complete contact information is available at: https://pubs.acs.org/10.1021/acsomega.4c01179

Notes

The authors declare no competing financial interest.

■ ACKNOWLEDGMENTS

We thank Lin-Zhe Lü at Xiamen University for helping with the Le Bail fitting and Dr. Zi-Ang Nan at the Xiamen Institute of Rare-Earth Materials for assistance in single-crystal structure analysis. We thank the financial support from the National Natural Science Foundation of China (22371280 and 52362021), the Natural Science Foundation of Fujian Province (2023H0046), the Jiangxi Provincial Natural Science Foundation (20224ACB204009), and the Youth Innovation Promotion Association CAS (2021302).

■ REFERENCES

(1) *AR6 Synthesis Report on Climate Change 2023*; The Intergovernmental Panel on Climate Change, 2023.

(2) Chow, J.; Kopp, R. J.; Portney, P. R. Energy resources and global development. *Science* **2003**, *302* (5650), 1528−1531.

(3) Wang, Z.; Li, C.; Domen, K. Recent developments in heterogeneous photocatalysts for solar-driven overall water splitting. *Chem. Soc. Rev.* **2019**, *48* (7), 2109−2125.

(4) Zhang, M.; Li, H.; Zhang, J.; Lv, H.; Yang, G.-Y. Research advances of light-driven hydrogen evolution using polyoxometalate-based catalysts. *Chin. J. Catal.* **2021**, *42* (6), 855−871.

(5) Fu, J.; Xu, Q.; Low, J.; Jiang, C.; Yu, J. Ultrathin 2D/2D WO3/g-C3N4 step-scheme H2-production photocatalyst. *Appl. Catal., B* **2019**, *243*, 556−565.

(6) Yu, M.; Zhang, N.; Xue, X.; Zhang, X.; Ren, X.; Feng, R.; Zhao, Y.; Sun, M.; Yan, T. Highly efficient visible-light photocatalytic hydrogen production using ZIF-derived Co9S8/N, S-CNTs-ZnIn2S4 composite. *Chem. Phys. Lett.* **2023**, *821*, 140470.
(7) Yuan, Y.-J.; Wang, P.; Li, Z.; Wu, Y.; Bai, W.; Su, Y.; Guan, J.; Wu, S.; Zhong, J.; Yu, Z.-T.; Zou, Z. The role of bandgap and interface in enhancing photocatalytic H2 generation activity of 2D-2D black phosphorus/MoS_2 photocatalyst. *Appl. Catal., B* **2019**, *242*, 1−8.
(8) Zheng, N.-C.; Ouyang, T.; Chen, Y.; Wang, Z.; Chen, D.-Y.; Liu, Z.-Q. Ultrathin CdS shell-sensitized hollow S-doped CeO_2 spheres for efficient visible-light photocatalysis. *Catal. Sci. Technol.* **2019**, *9* (6), 1357−1364.
(9) Hisatomi, T.; Domen, K. Reaction systems for solar hydrogen production via water splitting with particulate semiconductor photocatalysts. *Nat. Catal.* **2019**, *2* (5), 387−399.
(10) Zou, X. X.; Zhang, Y. Noble metal-free hydrogen evolution catalysts for water splitting. *Chem. Soc. Rev.* **2015**, *44* (15), 5148−5180.
(11) Kalyanasundaram, K.; Kiwi, J.; Gratzel, M. Hydrogen evolution from water by visible light, a homogeneous three component test system for redox catalysis. *Helv. Chim. Acta* **1978**, *61* (7), 2720−2730.
(12) Lang, M.; Borgmann, M.; Oberhuber, G.; Evstatiev, R.; Jimenez, K.; Dammann, K. W.; Jambrich, M.; Khare, V.; Campregher, C.; Ristl, R.; Gasche, C. Thymoquinone attenuates tumor growth in ApcMin mice by interference with Wnt-signaling. *Mol. Cancer* **2013**, *12*, 41.
(13) Blakemore, J. D.; Schley, N. D.; Olack, G. W.; Incarvito, C. D.; Brudvig, G. W.; Crabtree, R. H. Anodic deposition of a robust iridium-based water-oxidation catalyst from organometallic precursors. *Chem. Sci.* **2011**, *2* (1), 94−98.
(14) Du, P.; Eisenberg, R. Catalysts made of earth-abundant elements (Co, Ni, Fe) for water splitting: recent progress and future challenges. *Energy Environ. Sci.* **2012**, *5* (3), 6012−6021.
(15) Youngblood, W. J.; Lee, S.-H. A.; Kobayashi, Y.; Hernandez-Pagan, E. A.; Hoertz, P. G.; Moore, T. A.; Moore, A. L.; Gust, D.; Mallouk, T. E. Photoassisted overall water splitting in a visible light-absorbing dye-sensitized photoelectrochemical cell. *J. Am. Chem. Soc.* **2009**, *131* (3), 926−927.
(16) Yang, J.; Wang, D.; Han, H.; Li, C. Roles of cocatalysts in photocatalysis and photoelectrocatalysis. *Acc. Chem. Res.* **2013**, *46* (8), 1900−1909.
(17) Hunt, S. T.; Milina, M.; Alba-Rubio, A. C.; Hendon, C. H.; Dumesic, J. A.; Roman-Leshkov, Y. Self-assembly of noble metal monolayers on transition metal carbide nanoparticle catalysts. *Science* **2016**, *352* (6288), 974−978.
(18) Artero, V.; Fontecave, M. Solar fuels generation and molecular systems: is it homogeneous or heterogeneous catalysis? *Chem. Soc. Rev.* **2013**, *42* (6), 2338−2356.
(19) Cameron, J. M.; Guillemot, G.; Galambos, T.; Amin, S. S.; Hampson, E.; Mall Haidaraly, K.; Newton, G. N.; Izzet, G. Supramolecular assemblies of organo-functionalised hybrid polyoxometalates: from functional building blocks to hierarchical nanomaterials. *Chem. Soc. Rev.* **2022**, *51* (1), 293−328.
(20) Zeb, Z.; Huang, Y.; Chen, L.; Zhou, W.; Liao, M.; Jiang, Y.; Li, H.; Wang, L.; Wang, L.; Wang, H.; et al. Comprehensive overview of polyoxometalates for electrocatalytic hydrogen evolution reaction. *Coord. Chem. Rev.* **2023**, *482*, 215058.
(21) Canon-Mancisidor, W.; Paredes-Castillo, G.; Hermosilla-Ibanez, P.; Venegas-Yazigi, D.; Cador, O.; Le Guennic, B.; Pointillart, F. Role of the templating heteroatom on both structural and magnetic properties of POM-based SIM lanthanoid complexes. *Eur. J. Inorg. Chem.* **2021**, *2021* (45), 4596−4609.
(22) Zhang, M.; Wei, Y.; Li, R.; Zhu, W.; Li, H.; Zhang, Q.; Wang, M.; Chen, X.; Li, H. Magnetic POM-based mesoporous silica for fast oxidation of aromatic sulfur compounds. *Fuel* **2017**, *209*, 545−551.
(23) Dashtian, K.; Shahsavarifar, S.; Usman, M.; Joseph, Y.; Ganjali, M. R.; Yin, Z.; Rahimi-Nasrabadi, M. A comprehensive review on advances in polyoxometalate based materials for electrochemical water splitting. *Coord. Chem. Rev.* **2024**, *504*, 215644.
(24) Chen, Q.; Xiao, Y.; Xiao, F.-X. Crafting insulating polymer mediated and atomically precise metal nanoclusters photosensitized photosystems towards solar water oxidization. *Inorg. Chem.* **2024**, *63* (2), 1471−1479.
(25) Lentink, S.; Salazar Marcano, D. E.; Moussawi, M. A.; Parac-Vogt, T. N. Exploiting interactions between polyoxometalates and proteins for applications in (bio)chemistry and medicine. *Angew. Chem., Int. Ed.* **2023**, *62*, No. e202303817.
(26) Panagiotopoulos, A.; Douvas, A. M.; Argitis, P.; Coutsolelos, A. G. Porphyrin-sensitized evolution of hydrogen using Dawson and Keplerate polyoxometalate photocatalysts. *ChemSusChem* **2016**, *9* (22), 3213−3219.
(27) Sun, W.; An, B.; Qi, B.; Liu, T.; Jin, M.; Duan, C. Dual-excitation polyoxometalate-based frameworks for one-pot light-driven hydrogen evolution and oxidative dehydrogenation. *ACS Appl. Mater. Interfaces* **2018**, *10* (16), 13462−13469.
(28) Zhang, Z.-M.; Zhang, T.; Wang, C.; Lin, Z.; Long, L.-S.; Lin, W. Photosensitizing metal-organic framework enabling visible-light-driven proton reduction by a Wells-Dawson-type polyoxometalate. *J. Am. Chem. Soc.* **2015**, *137* (9), 3197−3200.
(29) Li, H.; Yao, S.; Wu, H.-L.; Qu, J.-Y.; Zhang, Z.-M.; Lu, T.-B.; Lin, W.; Wang, E.-B. Charge-regulated sequential adsorption of anionic catalysts and cationic photosensitizers into metal-organic frameworks enhances photocatalytic proton reduction. *Appl. Catal., B* **2018**, *224*, 46−52.
(30) Chen, X.; Li, C.; Grätzel, M.; Kostecki, R.; Mao, S. S. Nanomaterials for renewable energy production and storage. *Chem. Soc. Rev.* **2012**, *41* (23), 7909−7937.
(31) Chen, X.; Shen, S.; Guo, L.; Mao, S. S. Semiconductor-based photocatalytic hydrogen generation. *Chem. Rev.* **2010**, *110* (11), 6503−6570.
(32) Yamase, T. Hydrogen production by ultraviolet irradiation of alkylammonium polytungstate in neutral aqueous solutions. *Inorg. Chim. Acta* **1982**, *64* (3), L155−L156.
(33) Darwent, J. R. Photocatalytic hydrogen evolution from alcohols using dodecawolframosilicic acid colloidal platinum. *J. Chem. Soc.* **1982**, No. 14, 798−799.
(34) Lee, M. G.; Yang, J. W.; Kwon, H. R.; Jang, H. W. Crystal facet and phase engineering for advanced water splitting. *CrystEngComm* **2022**, *24* (33), 5838−5864.
(35) Raj, P.; Singh, A.; Singh, A.; Singh, A.; Garg, N.; Kaur, N.; Singh, N. Pyrophosphate prompted aggregation-induced emission: chemosensor studies, cell imaging, cytotoxicity, and hydrolysis of the phosphoester bond with alkaline phosphatase. *Eur. J. Inorg. Chem.* **2019**, *2019* (5), 628−638.
(36) Ren, C.; Li, J.; Zhang, X.; Niu, Y. Synthesis and photocatalytic properties of four coordination compounds constructed from two benzimidazole-based asymmetric polyazocyclic ligands. *Molecules* **2023**, *28* (9), 3841.
(37) Semwal, S.; Choudhury, J. Switch in catalyst state: single bifunctional bi-state catalyst for two different reactions. *Angew. Chem., Int. Ed.* **2017**, *56* (20), 5556−5560.
(38) Lu, T.; Xu, X.; Li, H.; Li, Z.; Zhang, X.; Ou, J.; Mei, M. The loading of coordination complex modified polyoxometalate nanobelts on activated carbon fiber: a feasible strategy to obtain visible light active and highly efficient polyoxometalate based photocatalysts. *Dalton Trans.* **2015**, *44* (5), 2267−2275.
(39) Liu, H.-Y.; Yang, J.; Liu, Y.-Y.; Ma, J.-F. pH-Dependent assembly of two inorganic-organic hybrid compounds based on octamolybdates: an unusual intercalated layer and a 3D 4-connected framework. *Dalton Trans.* **2012**, *41* (33), 9922.
(40) Mbomekalle, I. M.; Lu, Y. W.; Keita, B.; Nadjo, L. Simple, high yield and reagent-saving synthesis of pure α-$K_6P_2W_{18}O_{62}\cdot 14H_2O$. *Inorg. Chem. Commun.* **2004**, *7* (1), 86−90.
(41) Dolomanov, O. V.; Bourhis, L. J.; Gildea, R. J.; Howard, J. A. K.; Puschmann, H. OLEX2: a complete structure solution, refinement and analysis program. *J. Appl. Crystallogr.* **2009**, *42*, 339−341.
(42) Sheldrick, G. M. Crystal structure refinement with SHELXL. *Acta Crystallogr., Sect. C: Struct. Chem.* **2015**, *71*, 3−8.
(43) Spek, A. L. Structure validation in chemical crystallography. *Acta Crystallogr., Sect. D: Struct. Biol.* **2009**, *65*, 148−155.

https://doi.org/10.1021/acsomega.4c01179
ACS Omega 2024, 9, 18556−18565

(44) Frisch, M. J.; Trucks, G. W.; Schlegel, H. B.; Scuseria, G. E.; Robb, M. A.; Cheeseman, J. R.; Scalmani, G.; Barone, V.; Petersson, G. A.; Nakatsuji, H. L. X.; Caricato, M.; Marenich, A. V.; Bloino, J.; Janesko, B. G.; Gomperts, R.; Mennucci, B.; Hratchian, H. P.; Ortiz, J. V.; Izmaylov, A. F.; Sonnenberg, J. L.; Williams; Ding, F.; Lipparini, F.; Egidi, F.; Goings, J.; Peng, B.; Petrone, A.; Henderson, T.; Ranasinghe, D.; Zakrzewski, V. G.; Gao, J.; Rega, N.; Zheng, G.; Liang, W.; Hada, M.; Ehara, M.; Toyota, K.; Fukuda, R.; Hasegawa, J.; Ishida, M.; Nakajima, T.; Honda, Y.; Kitao, O.; Nakai, H.; Vreven, T.; Throssell, K.; Montgomery, J. A., Jr.; Peralta, J. E.; Ogliaro, F.; Bearpark, M. J.; Heyd, J. J.; Brothers, E. N.; Kudin, K. N.; Staroverov, V. N.; Keith, T. A.; Kobayashi, R.; Normand, J.; Raghavachari, K.; Rendell, A. P.; Burant, J. C.; Iyengar, S. S.; Tomasi, J.; Cossi, M.; Millam, J. M.; Klene, M.; Adamo, C.; Cammi, R.; Ochterski, J. W.; Martin, R. L.; Morokuma, K.; Farkas, O.; Foresman, J. B.; Fox, D. J. *Gaussian 16*, Revision B.01: Wallingford, CT, 2016.

(45) Lu, T.; Chen, Q. Interaction region indicator: a simple real space function clearly revealing both chemical bonds and weak interactions. *Methods Chem.* **2021**, *1* (5), 231−239.

(46) Lu, T.; Chen, F. Multiwfn: a multifunctional wavefunction analyzer. *J. Comput. Chem.* **2012**, *33* (5), 580−592.

(47) Le Bail, A.; Duroy, H.; Fourquet, J. L. Ab-initio structure determination of $LiSbWO_6$ by X-ray powder diffraction. *Mater. Res. Bull.* **1988**, *23* (3), 447−452.

(48) Sen, B.; Paul, S.; Krukowski, P.; Kundu, D.; Das, S.; Banerjee, P.; Małecka, M.; Abbas, S. J.; Ali, S. I. $CuAs_2O_4$: design, hydrothermal synthesis, crystal structure, photocatalytic dye degradation, hydrogen evolution reaction, knoevenagel condensation reaction, and thermal studies. *Inorg. Chem.* **2024**, *63*, 2919−2933.

(49) Rodriguezcarvajal, J. Recent advances in magnetic structure determination by neutron powder diffraction. *Physica B* **1993**, *192* (1−2), 55−69.

(50) Liu, H.-Y.; Wu, H.; Yang, J.; Liu, Y.-Y.; Liu, B.; Liu, Y.-Y.; Ma, J.-F. pH-Dependent assembly of 1D to 3D octamolybdate hybrid materials based on a new flexible bis-(pyridyl)-benzimidazole ligand. *Cryst. Growth Des.* **2011**, *11* (7), 2920−2927.

(51) Park, S.; Jung, J.; Cho, E. J. Visible-light-promoted synthesis of benzimidazoles. *Eur. J. Org Chem.* **2014**, *2014* (19), 4148−4154.

(52) Wang, J.-Z.; Wang, T. How to interpret infrared (IR) spectra. *Univ. Chem.* **2016**, *31* (6), 90−97.

https://doi.org/10.1021/acsomega.4c01179
ACS Omega 2024, 9, 18556−18565